In situ 3D synchrotron laminography assessment of edge fracture in Dual-Phase steels: Quantitative and numerical analysis

M. Kahziz*[,1,2], T.F. Morgeneyer[1], M. Mazière[1], L. Helfen[3,4], O. Bouaziz[5] and E. Maire[6]

[1]MINES ParisTech, PSL Research University, Centre des Matériaux, CNRS UMR 7633, BP 87 91003 Evry, France
[2]ArcelorMittal Research, Voie Romaine-BP30320, 57283 Maizières-lès-Metz Cedex, France
[3]European Synchrotron Radiation Facility, 6 rue Jules Horowitz, BP 220, F-38043 Grenoble Cedex, France
[4]ANKA, Karlsruhe Institute of Technology (KIT), D-76131 Karlsruhe, Germany
[5]Université de Lorraine, LEM3, UMR CNRS 7239, F-57045 Metz Cedex 01, France
[6]INSA-Lyon, MATEIS CNRS UMR 5510, 7 Avenue Jean Capelle, 69621 Villeurbanne, France

Abstract

The mechanical performance of automotive structures made of advanced high strength steels (AHSS) is often seen reduced by the presence of cut edges. An attempt is made to assess and quantify the initial damage state and the damage evolution during mechanical testing of a punched edge and a machined edge via a recently developed 3D imaging technique called synchrotron radiation computed laminography. This technique allows us to observe damage in regions of interest in thin sheet-like objects at micrometer resolution. In terms of new experimental mechanics, steel sheets having sizes and mechanical boundary conditions of engineering relevance can be tested for the first time with *in situ* 3D damage observation and quantification. It is found for the investigated DP600 steel that the fracture zone of the punched edge is rough and that needle-shape voids at the surface and in the bulk follow ferrite-martensite flow lines. During mechanical *in situ* testing the needle voids grow from the fracture zone surface and coalesce with the sheared zone. In contrast, during *in situ* mechanical testing of a machined edge the damage starts away from the edge ($\sim 800\mu m$) where substantial necking has occurred. Three-dimensional image analysis was performed to quantify the initial damage and its evolution. These data can be used as input and validation data for micromechanical damage models. To interpret the experimental findings in terms of mechanical fields, combined surface digital image correlation and 3D finite element analysis were carried out using an elasto-plastic constitutive law of the investigated DP steel. The stress triaxiality and the accumulated plastic strain were calculated in order to understand the influence of the edge profile and the hardening of the cutting-affected zone on the mechanical fields.

Keywords: DP steels, ductile damage, edge fracture, synchrotron laminography and FE analysis

*Corresponding author at: MINES ParisTech, PSL Research University,MAT - Centre des Matériaux, CNRS UMR 7633, BP 87 91003 Evry, France. Email address: mouhcine.kahziz@mines-paristech.org. Tel.: +33 160763069; fax: +33 160763150.

DOI: 10.1007/s11340-015-0076-3

1 Introduction

Advanced High Strength Steels (AHSS) grades are, beside other steel grades (as e.g. HSLA, bake hardenable...), widely used and developed materials in the automotive industry for environmental and safety reasons. Among these AHSS grades, dual phase (DP) steels with their ferrite-martensite composite microstructure present a good compromise between strength and formability. However, forming processes can affect the mechanical behavior of these grades. In automotive industry, the operations based on shearing and punching are the most used cutting processes due to their speed, simplicity and low cost. Cases of failure in DP steels, which initiate via ductile fracture mechanisms on blanked edges were detected [1]. This may lead to a drop in the mechanical performance of automotive parts and therefore of the vehicle safety [1]. It was shown that the cutting step can alter the mechanical properties of this grade [1–3]. These studies have shown that the cutting process of DP sheets affects the adjacent material that extends into the bulk region of the sheet. While ductile fracture mechanisms of this steel and its base materials (i.e. ferrite and martensite separately) were discussed in the past (see [6, 13, 54, 69] and others), the mechanisms of edge fracture in DP steels are not well known.

It is found for DP steels that the failure is governed by ductile damage mechanisms, e.g. void nucleation, growth and coalescence phenomena. Damage nucleation in dual phase steels was investigated in several studies [4–10]. Void formation in DP steels is mainly due to the ferrite/martensite interface decohesion, or to the fracture of the martensite particles. The growth of cavities in steels is evidenced in the literature using different microstructural characterization techniques like metallographic observation [7, 11, 12]. There are only few experimental works on void coalescence in dual phase steels due to the difficulty to observe this ductile damage stage. Using X-ray tomography, Landron and co-workers [13] have qualitatively assessed the void coalescence stage in a DP steel during *in situ* tensile test. The models of Brown and Embury [14] and of Thomason [15] were identified in order to predict the void coalescence in the studied DP steel.

Several models were developed to model the initiation and the evolution of ductile damage in DP steels. The most used approach to model the void nucleation were proposed by Argon [16], by Beremin [17] and by Chu and Needleman [18]. These models do, however, not explicitly account for ferrite-martensite decohesion. Rice and Tracey's model [19] and Huang's model [20] allow one to model the void growth taking into account the stress triaxiality and the plastic strain effect. Gurson [21] has proposed an equation of the yield surface depending on volume fraction of the porosity dedicated to the porous media to model the growth of a spherical cavity in an infinite matrix assuming that the matrix is isotropic, rigid and perfectly plastic. Ben-Bettaieb *et al.* [22] and Fansi *et al.* [23] have developed a modified GTN (GursonTvergaardNeedleman) model which integrates physically based void nucleation and growth laws. The reader interested in GTN model and its extension should refer to [24].

Many experimental works were performed to understand the influence of cutting processes conditions on the formed edges (see [25–28] and others). The edge profile depends heavily on many parameters such as the material behavior, the clearance, the cutting speed [28–37]. In the last decades several works linking experimental approaches and numerical methods were carried out on that topic (e.g. [28, 31, 38–41]).

Tensile tests on samples containing sheared edges were used to investigate the sheared edges ductility [[1]]. However, during this test, necking occurred before the sheared edge fracture which makes the deformation analysis more complicated. The hole expansion test which is controlled by visual inspection was performed in many studies in order to investigate the local formability of punched edges [42–44]. In [45], a study of three different edge conditions (milled edge, water jet cut edge and punched edge) was performed using hole expansion test. It was found that the punched edge exhibits the lowest hole expansion ratio (HER) compared to the two others investigated edges. However, this test is sensitive to the sample geometry and microstructure [44]. Indeed, the important scattering in results observed for this test limits its use. In [46],it has been observed that during hole expansion, cracks were mainly initiated at the fracture surface and the cracks became longer and deeper from the punched surface with the increase of hole expansion ratio. A new test was developed by Bouaziz and co-workers [47] called double bending to investigate the sheared edges ductility which allows one to separate necking and damage behaviors by localizing the strain on the sheared edge. Using this test the sheared edge fracture is achieved without any necking and the strain field can be continuously determined by an image correlation system.

Few studies are available in the literature on the cut edges mechanical behavior and the mechanisms of edge fracture. Thomas *et al.* [2] and Lara *et al.* [3] have investigated the influence of shearing and laser cut edge characteristics on the fatigue life performance of high strength automotive steels. In their recent study focused on failure during sheared edge stretching of DP steels, Levy *et al.* [48] observed that increased strength of martensite retards crack initiation from a sheared edge. Crack growth was found to be made easier with increasing surface fraction of martensite/ferrite interfaces. Additionally, increased strain hardening was found to lead to void formation at low macro strain. In the studies performed by Levy and co-workers [49, 50], it was concluded that local deformation in the shear-affected zone in DP steels is the main factor controlling the failure during sheared-edge stretching.

Recent in situ X-ray synchrotron non-destructive techniques were developed to assess the ductile damage evolution. Synchrotron tomography, especially adapted to compact or one-dimensionally elongated objects which stay in the field of view of the detector system under rotation, was used in several studies to observe in 3D and in situ the ductile damage initiation and evolution in DP steels [6, 13, 51–54]. Synchrotron laminography was developed for 3D imaging [55–57] of regions of interest (ROI) in plate-like specimens that are extended in two dimensions which provides a unique way to qualitatively and quantitatively assess damage and its evolution in sheet materials [58, 59]. This technique was used in several studies to observe in 3D the ductile damage evolution in Aluminium alloys [60–62]. Morgeneyer and co-workers [63] have combined in situ synchrotron laminography with digital volume correlation in order to measure in 3D the displacement and strain fields during the tensile test of a notched sample.

The present study aims at providing quantitative information about the microstructural initial state of a punched edge and a machined edge in terms off damage and its evolution. In situ synchrotron laminography was used during simultaneous bending and tensile mechanical loading of samples containing a punched hole and an EDM (electrical discharge machining) machined hole. Here, three-dimensional laminography has been used for the first time to assess the damage evolution in steel sheets. The use of large specimens (several tens of mm in width and height) is an advantage over tomography at micrometre resolution: relevant large plastic zones can develop during the mechanical test using laminography as it is the case in forming processes. These techniques could also be applied to weldments [64] and valuable information could be gained if micrometre sized defects play a role [65]. Quantitative image analysis of laminography data was performed in order to understand the ductile damage evolution during edge fracture. Surface digital image correlation (DIC) was carried out using the software Correli^{Q4} in order to measure the displacement fields in the region of interest. These are used for comparison and as input data for FE simulations. A 3D finite element analysis was performed using an elasto-plastic constitutive law of the investigated DP steel to interpret the behavior of the punched and machined edges in terms of mechanical fields.

2 Experimental methods

2.1 Material

The material investigated in this study is a laboratory dual phase steel (fig. 2.1) with an ultimate tensile strength of approximately 600 MPa and a fracture elongation around 20% in the as-received condition. The martensite surface fraction measured on scanning electron microscopy images was about 20%. This value is slightly overestimated due to the presence of some carbides and grain boundaries that are included in this surface fraction. The material was supplied as a 0.8 mm thick cold rolled sheet. The main alloying elements are: C (0.095), Mn (1.89) and Si (0.24) in weight%. The micrograph in fig. 2.1 shows that martensite islands appear to be aligned along the rolling direction. In the following the rolling direction will be referred to as L, the long transverse direction as T and the short transverse direction as S for all experiments presented in this work. The loading configuration was T-L, the first letter corresponds to the loading direction and the second to the crack propagation direction.

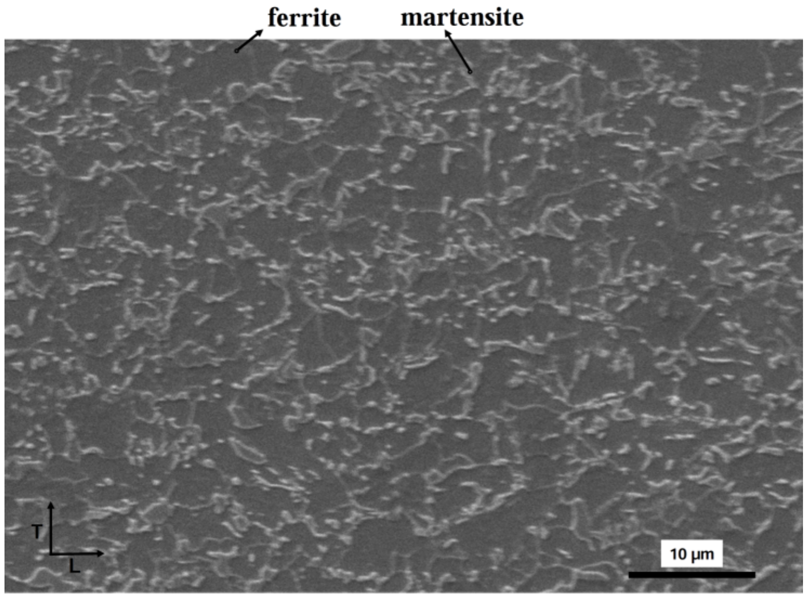

Figure 2.1: DP microstructure visualized by scanning electron microscopy (after polishing and 2% nital etching)

2.2 The punched edge profile

The shearing process, which is a cutting in a straight line over the entire width of the sheet by the action of a moving blade perpendicular to the plane of the sheet, is the most widely used and least expensive process for sheet cutting. The punching process produces edge profiles that are similar to the ones produced by shearing processes. In this paper, a punched edge, which was produced with a clearance of 15%, is investigated. This ratio is defined as the distance between the blades divided by the sheet thickness. The value used here is a typical value in automotive industry. Fig. 2.2(a) shows an optical micrograph of the polished surface of a punched edge after the cutting process. Flow lines shown in Fig. 2.2(a) induced by the cutting process are defined by grain (martensite) orientation. The edge profile is characterized by the existence of four zones: rollover zone, sheared zone, fracture zone, and burr zone (fig. 2.2(a)). The punched edge hardening profile shown in Fig. 2.2(b) has been measued by the Vickers microindentation method using a load of $50g$. The hardening was then calculated using the following formula:

$$Hardening[\%] = \frac{HV_l - HV_\infty}{HV_\infty} \times 100 \tag{1}$$

Where HV_l is the microhardness measured at the distance l from the edge surface and HV_∞ is the base material microhardness. An increased hardness in the cutting-affected zone can be seen. This profile will be taken into account in further numerical analysis in order to study the pre-straining effect.

The fracture zone displays the highest damage and presents a high roughness in agreement with the findings in [32]. Some zones of decohesion at the ferrite-martensite interfaces can be observed in the fracture zone and are aligned along the flow lines. This had been already observed in [1].

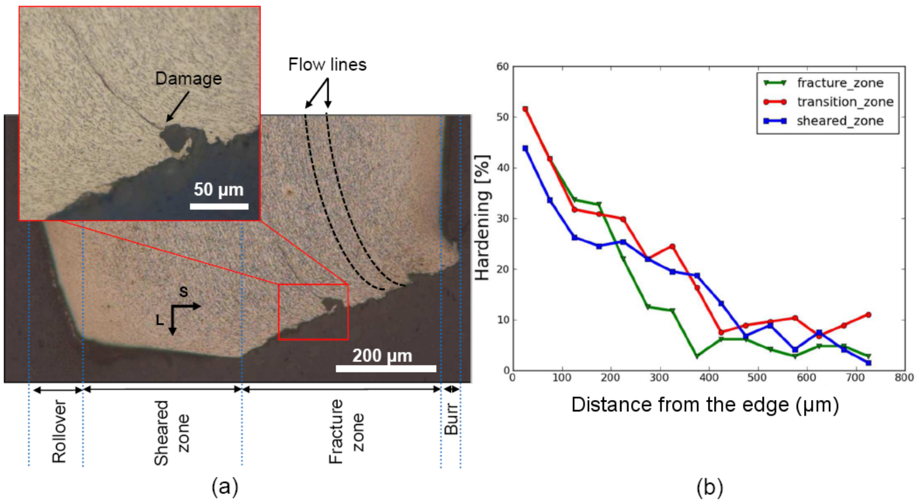

Figure 2.2: (a) Optical Microscopy of a punched edge profile using a clearance ratio of 15%, etched in 2%-Nital showing the orientation of flow lines and a microcrack in the fracture zone. (b) hardening profile along L direction on the investigated punched edge measured by Vickers microhardeness technique in the fracture zone, sheared zone in the transition zone between both.

2.3 In situ laminography and mechanical testing

The laminography experiments were performed at the ID19 beam line of the European Synchrotron Radiation Facility (ESRF) in Grenoble, France. The acquisition of projection images was performed employing a filtered white beam (centered around a $60keV$ X-ray energy) and using a high-dose detector system [66] with an isotropic voxel size of $(0.778\mu m)^3$. The rotation axis inclination angle on the laminography device was chosen to around 30° (= θ - 90°). A simultaneous diffraction experiment was not carried out as this would require a lot more X-ray beamtime and a more complex experimental setup.

The sample geometry shown in fig. 2.3(a-b) was used. A hole with a radius of $5mm$ was punched out from a sheet of DP steel and an elongated notch was machined up to one edge. For the case of the machined edge the hole radius was $6mm$. The EDM (electrical discharge machining) machined edge surface was polished in order to eliminate the EDM wire cutting affected zone. The loading was applied perpendicular to the notch, via a two-screw displacement-controlled wedging device that allows us to incrementally open the notch and control the specimen crack mouth opening displacement (CMOD) similar to the one used in [60] and [61]. To avoid the sample buckling and out-of-plane motion, an anti-buckling device was used. The entire rig was mounted in a dedicated plate that was removed from the laminography rotation stage between loading steps (see fig. 2.3(c)). After each loading step, a scan of the region of interest (ROI) containing the crack tip was carried out and a 2D surface picture was taken for digital image correlation (DIC) that can be used as optical extensometer to know the displacement field around the ROI.

A filtering operation was performed using a 3D median filter with a radius of 2 voxels in order to reduce the noise of the reconstructed images. An automatic threshold (Auto-thresholding) calculated from the histogram of the gray levels was used on the median-filtered volumes to create the binary images. The edge surface was detected using a plug-in implemented in ImageJ freeware ([68]) based on Sobel edge detector that consists in highlighting sharp changes in intensity in 3D binarized volumes. The 3D visualization was done using ImageJ 3D volume viewer. In this work, voids and edge surface always appear in blue and the material bulk in white. A scanning electron microscopy with X-ray micro-analysis (SEM/EDS) was carried out on a 4 mm^2 L-S section. It has shown that the investigated material contains three types of inclusions (MnS, CaO and Al_20_3) which are not all detectable using X-ray laminography. The image contrast is mainly due to absorption contrast, i.e. a density difference of the objects is needed to obtain a gray level difference in the 3D image. If particles and matrix have a similar density, the phases may not be distinguished. In addition if the particles are smaller than the voxel size (0.778 μm) they cannot be detected. The inclusion surface fraction measured in the observed surface was 0.08%.

It is important to mention that X-ray laminography does not allow to distinguish the ferritic phase from the martensitic one because the attenuation coefficients of the two phases are very close.

The in situ X-ray synchrotron laminography of the machined edge has offered low noise observations with a better signal/noise ratio than the punched edge observation experiment. The two observations were carried out using the same X-ray energy and the same resolution (isotropic voxel of $(0.778\mu m)^3$).

The experimental conditions had a higher signal/noise ratio for the punched edge scans than the observation of the machined edge performed during a later experiment. This has induced noise (artefacts) in the reconstructed data.

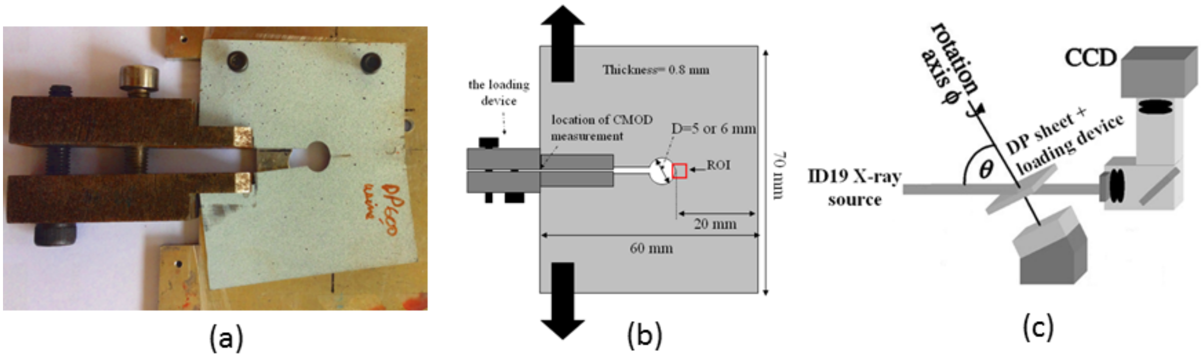

Figure 2.3: In situ mechanical testing: (a) photograph of the loading device and specimen mounted on one of the two anti buckling plates (b) schematic drawing of the specimen geometry, the loading and crack growth directions and the region of interest (ROI). (c) schematic drawing of X-ray KIT synchrotron laminography installed at ID19 beam-line at the ESRF Grenoble [55]

2.4 Method and tools for the post processing

2.4.1 Reconstruction and visualization

Synchrotron laminography scans were reconstructed using a filtered back-projection (FBP) algorithm adapted to the computed laminography acquisition geometry [67]. The reconstructed data is processed here in order to analyze qualitatively and quantitatively the mechanisms of edge fracture. All the processing operations are carried out using ImageJ dedicated to image processing [68].

2.4.2 Quantification of the initial state of punched and machined edge

Two sub-volumes $(310\mu m)^3$ were extracted from the reconstructed data of the machined edge and the punched edge at the initial state to calculate the mean value of void volume fraction and the distribution of voids using a home made plug-in implemented in ImageJ that detects and labels each pore which must be a cluster of at least three connected voxels to be considered. These sub-volumes were extracted away from the edge in order to avoid the cutting affected zone for the punched and machined edges. The average values of combined detectable particle volume fraction (PVF) and void volume fraction (VVF) found for the $(300\mu m)^3$ analyzed sub-volumes were 0.021% and 0.045% for the punched edge and machined edge respectively. As mentioned in [69] the resolution has an important influence on the damage measurement. The observation performed on a DP steel at very high resolution (voxel of $(0.1\mu m)^3$) showed that a large

DOI: 10.1007/s11340-015-0076-3

part of damage is not detected at low resolution (voxel of $(1.6\mu m)^3$). Some small sub-micrometre features may not be detected here as they are smaller than the achieved resolution (voxel of $(0.778\mu m)^3$).

Fig. 2.4(a) shows the histogram of void size for the two sub-volumes (punched and machined edge) analyzed via in situ laminography in the as-delivered state.

Fig. 2.4(b) shows the profile of VVF (see next section for exact definition) as a function of the distance from the edge surface for the investigated edges in the as-received state. We observed that there are two times less cavities in the punched edge far from the edge than for the machined edge. This is due to the less good signal-to-noise ratio during the experiment for the punched edge. In order to improve the quantification of the initial state of punched edge and to better quantify the damage at the initial state, a second punched edge was observed via the laminography set-up located at ID15 beam-line at ESRF Grenoble. The observation was performed using a resolution of $1.1\mu m$. The average VVF value measured in a ($310\times310\times310$ μm^3) volume extracted far from the cutting-affected zone was 0.051%. The evolution of VVF in this punched edge is given in fig. 2.4(b) (punched edge 2). It shows that the damage (voids) is higher near the edge surface and it shows the same level as the machined edge away from it.

2.4.3 Quantification of void evolution by discretisation of the volume

To analyze quantitatively the 3D reconstructed laminography data, an in-house code based on Python [70] was used on median-filtered and binarized sub-volumes of ($1200\times300\times300\mu m^3$) in order to calculate the distribution of void volume fraction in the machined edge. For the case of the punched edge the analyzed sub-volumes were of ($600\times300\times300\mu m^3$) including the edge surface in order to avoid the artefacts in the center of the image. This code discretizes the studied sub-volumes into boxes of $(50\ \mu m)^3$, in each box the void volume fraction (VVF) is calculated. For each elements column in the T direction, the maximum VVF value was calculated, named $max_T(VVF)$, assuming that the highest level of damage will be the most detrimental to structural integrity. Fig. 2.4(c) shows the maximum measured VVF in loading direction (T), $max_T(VVF)$, in discretized boxes ahead of the machined edge. The spatially heterogeneous distribution of $max_T(VVF)$, can be observed in this unloaded state. The average value of $max_T(VVF)$ was determined along the short transverse direction S (green lines in fig. 2.4(c)) resulting in $< max_T(VVF) >_S$.

2.4.4 2D digital image correlation

The in situ test was performed at the synchrotron facility with the already described simple loading device that does not allow to determine the displacement applied during notch opening. Surface digital image correlation (DIC) was carried out using the software called Correli^{Q4} implemented in Matlab^{TM} in order to measure the displacement and strain fields in the region of interest ([71]). In this correlation code a global approach is used in which the ROI is discretized in four-noded elements rather than in sub-sets as in the local approaches. In the global approach the continuity of the displacement fields is assumed. We used a Basler Pilot (piA2400-17gm) camera in a single shot mode for each load step with an exposure time of 50 ms. The pixel size was 2.59 μm. Between loading steps, images were taken in the region of interest where a spray paint speckle was applied on the specimen surface. The DIC was performed by updating the reference image and using an element size of $180\times180\mu m^2$ and a ROI of $2\times4mm^2$.

3 Experimental results

3.1 The punched edge

Fig. 3.5 shows the 2D sections taken at $320\mu m$ from the edge of reconstructed laminography raw data (before filtering and binarization) at different loading steps in the fracture zone of the specimen. The ferrite

DOI: 10.1007/s11340-015-0076-3

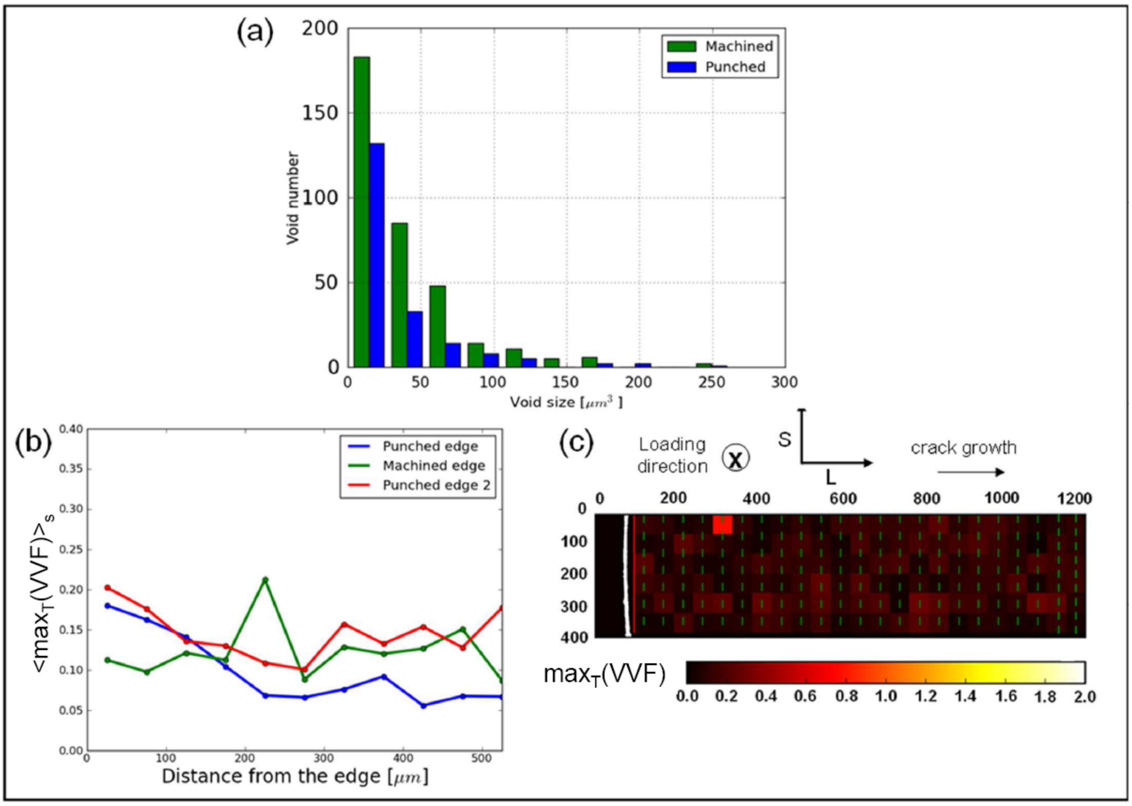

Figure 2.4: (a) Void size distribution in a 3D sub-volume of 310×310×310μm^3 for punched edge and machined edge; (b) $< max_T(VVF) >_S$ distribution at the initial state in punched and machined edges and the VVF mean values found for sub-volumes of 310×310×310μm^3; (c) cartography of void distribution in the machined edge at the initial state using the in-house Python code (dimensions are in μm).

and martensite are shown in gray and the initial internal voids can be seen in black in the matrix. Ring artefacts that are not present for scans of the machined edge can be seen in the 2D sections of reconstructed data in fig. 3.5. Fig.3.5(a) shows a sketch illustrating the geometry of the observed specimen, the ROI for laminography which was about 1 mm^3 and the loading and crack growth directions. In the initial state, i.e. after punching and before mechanical testing of the hole, the roughness of the fracture zone and a geometrical defect caused by the punching process can be seen along the punched edge in fig. 3.5(b). The defect consists in a geometrical step with a height in the order of 30μm. A cavity is formed at 50μm ahead of the crack tip. Laminography artifacts that appear in fig. 3.5(b) do not influence strongly the segmentation of the voids. The 2D section in fig. 3.5(d) taken at CMOD=4 mm shows that a microcrack initiates on the edge surface. A second crack that appears close to a geometrical defect can be seen in 3.5(d). In the 2D section given in fig. 3.5(e) corresponding to CMOD=4.5 mm, we can see the growth of the cavity formed in front of the crack. The 2D section given in 3.5(f) shows the coalescence of the crack and the void formed ahead of it via narrow void sheet and that the crack located close to the geometrical defect grows faster. This is consistent with the increased level of stress triaxiality caused by the geometrical defect. The void coalescence sheets are inclined at about 45° compared to the loading direction (see fig. 3.5(e)).

Thanks to X-ray laminography it is possible to visualize the damage evolution in three dimensions. Fig. 3.6 shows regions of 1240×930×310μm^3 taken at different CMODs. The voids and the edge surface segmented and visualized in L-T plane, are shown in blue. Ferrite and martensite appear transparent. Fig. 3.6(b) shows the as-received material after punching. The fracture and sheared zone surfaces and the geometrical defect located in the fracture-to-sheared transition zone can be seen in fig. 3.6(b). The

DOI: 10.1007/s11340-015-0076-3

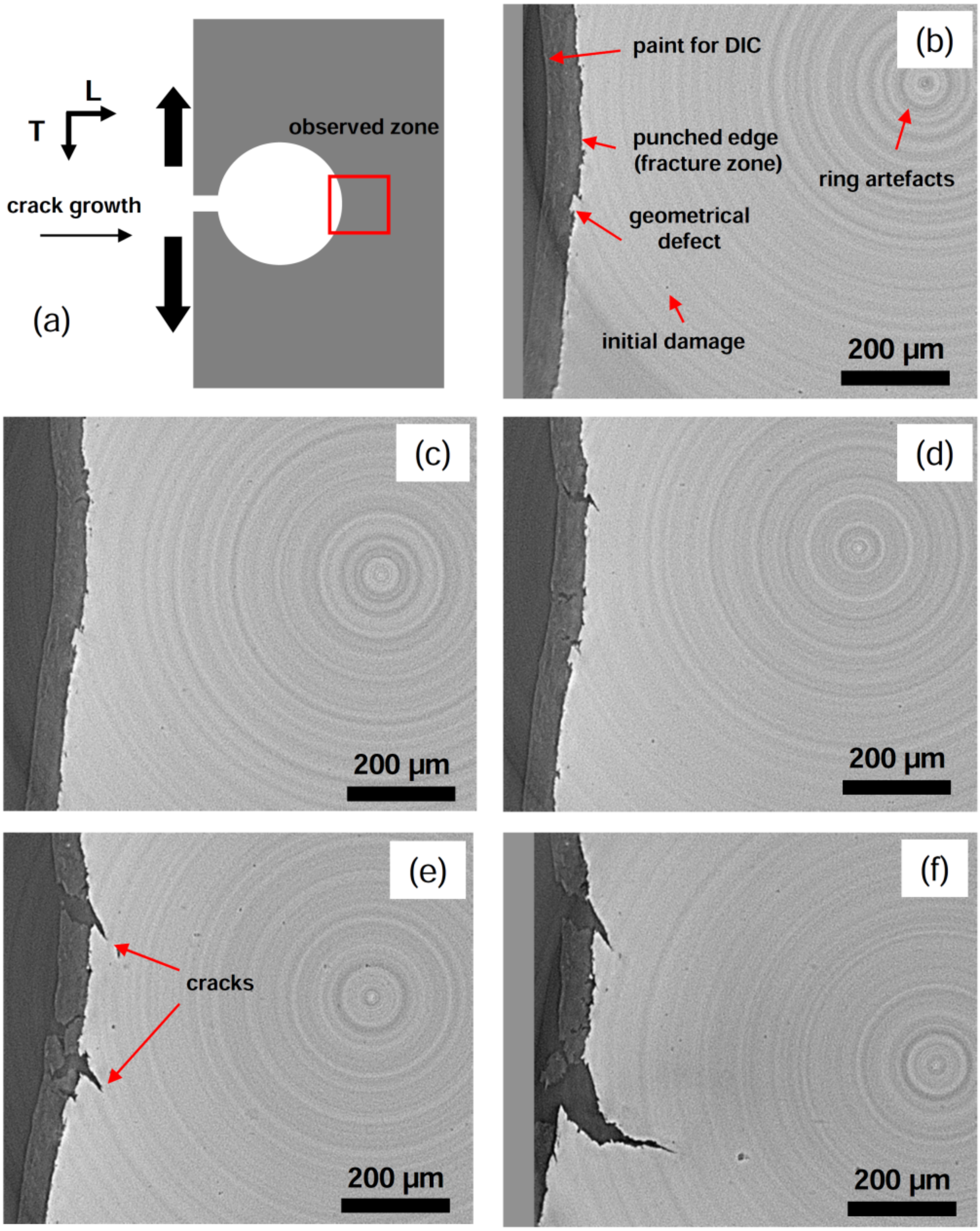

Figure 3.5: 2D sections of laminography data taken at the fracture zone at $320\mu m$ from the edge surface of the sheet plane of reconstructed laminography data showing damage evolution from a punched edge at different CMODs (a) schematic drawing illustrating specimen geometry, ROI location and loading and crack growth directions (b) material at delivery state; (c) CMOD=$3mm$; (d) CMOD=$4mm$; (e) CMOD=$4.5mm$; (f) CMOD=$5mm$.

3D section in fig. 3.6(d) shows the two cracks observed in the 2D section (3.5(d) corresponding to CMOD=$3mm$) formed in the fracture zone surface especially the one initiated close to the geometrical defect. A third crack which was not observed in the 2D sections presented in fig. 3.5 can be seen in 3.6(d) at the fracture-to-sheared transition zone inclined at 45° compared to the loading direction. We also observe the initiation of other cracks in the fracture zone surface and in the fracture-to-sheared transition zone (fig. 3.6(d) taken at CMOD=4mm). All the cracks are oriented at 45° with respect to the loading direction. Fig. 3.6(e) taken at CMOD=4.5mm shows the crack growth and coalescence with the sheared zone surface via narrow coalescence sheets. The void growth near the edge surface is higher than in the bulk material (fig. 3.6(e)). In fig. 3.6(f), the final crack that crosses the specimen thickness and leads to the edge fracture is formed by the growth of the crack initially initiated close to the geometrical defect that acted as a stress concentration and the coalescence with the internal voids formed ahead of the crack. However, the mechanisms of crack growth remain the same for all the formed cracks.

The 3D volumes given in fig. 3.7 are the same as those observed in fig. 3.6 but seen from the side of the sheet. These 3D observations of a 330×390×210μm^3 zone extracted at mid-thickness of the specimen show the fracture and sheared zones with a view along the loading direction. Fig. 3.7(b) shows the voids nucleated close to the edge surface which are aligned along the martensite islands microstructural alignment (flow lines) during the punching process. The roughness of the fracture zone surface can also be seen (fig. 3.7(b)). The 3D volume at CMOD=2mm (fig. 3.7(c)) shows the growth of the pre-existing voids and the nucleation of new ones. A "needle shape" void formed close to the geometrical defect grows perpendicular to the sheared zone surface. The coalescence of the needle void formed close to the geometrical defect with the sheared zone surface occurred via a narrow coalescence sheet, and formed a crack at 45° with respect to the loading direction (fig. 3.7(d)). To the best of our knowledge, these observations of ductile crack propagation from a punched edge and coalescence with internal voids in the material bulk have never been observed before with such a high level of details and in situ. The 3D volume given in fig. 3.7(e) at CMOD=4mm shows the growth and the coalescence of voids following the flow lines corresponding to the martensite island alignment. Fig. 3.7(f) shows that the coalescence of the formed crack with the void clusters occurred at the crack tip.

3.2 The machined edge

The fig. 3.8 shows the 2D sections taken at mid-thickness of reconstructed laminography raw data (before filtering and binarization) for a machined edge specimen. We observe that these experiments do not present strong characteristic laminography artifacts. This is due to the fact that these acquisitions were performed later and with much better signal-to-noise ratio than those shown earlier for the punched edge. The fracture process revealed by these observations for the EDM machined edge is very different from the punched edge described above. The 2D sections in fig. 3.8(c) and (d) taken at CMOD= 3mm and 5.5mm respectively show that the damage nucleation and growth seem to be homogeneous. However, in the fig. 3.8(e), we observe a high damage amount leading to the formation of a cluster of aligned voids away from the edge surface which leads to the final crack shown in 3.8(f).

Fig. 3.9 shows the 3D volumes (1240×310×310μm^3) extracted at mid-thickness of post processed laminography data of damage evolution during the EDM machined edge loading. The 3D volume given in fig. 3.9(b) shows the machined edge in as-received state. The voids seem to be homogeneously distributed in the bulk material unlike the punched edge which presents an increased damage close to the edge surface. The damage growth seems to be homogeneous in the 3D volume given in fig. 3.9(c) which corresponds to CMOD=3mm. Fig. 3.9(d) at CMOD= 6.25mm shows the nucleation and growth of a new void population. The damage growth was higher in the bulk material away from the edge surface which is explained by the increased level of stress triaxiality in the bulk material (fig. 3.9(e) corresponding to CMOD=7.25mm). The crack leading to the final fracture occurred away from the edge surface (fig. 3.9(f) at CMOD=7.75mm). It was the result of the coalescence of voids nucleating and growing at least 1000μm away from the edge surface. We note that at the state presented in fig. 3.9(f), the crack close to the edge is still closed.

Fig. 3.10 shows the 2D minimal sections of the reconstructed laminography data shown in fig. 3.9 taken

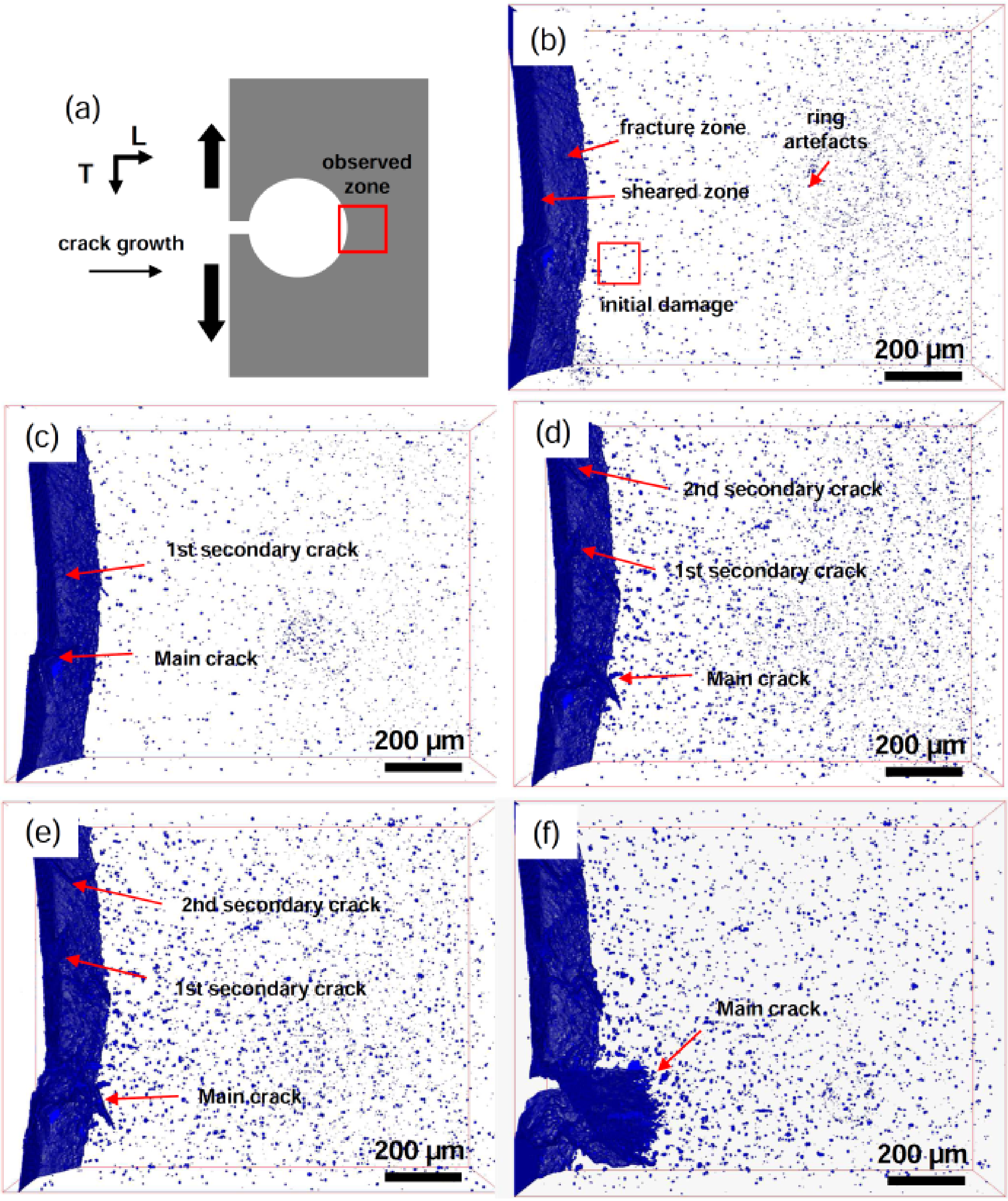

Figure 3.6: 3D volumes of the reconstructed laminography data showing a region of $1240 \times 930 \times 310 \mu m^3$ in the L-T plane at mid-thickness of the damage evolution from a punched edge at different CMODs. Voids, specimen surface and the crack are shown in blue. The steel matrix is made transparent (a) schematic drawing illustrating specimen geometry at the punched hole, observed area location and loading and crack growth directions; (b) material at delivery state; (c) CMOD $= 3mm$; (d) CMOD$=4mm$; (e) CMOD$=4.5mm$; (f) CMOD$=5mm$.

in the L-S plane. The initial specimen thickness was $0.8mm$. At CMOD$=5.5mm$ (fig. 3.10(b)), the deformation was homogeneously distributed in the specimen thickness. Necking was measured at the location of minimum thickness. In fig. 3.10(b), homogeneous necking of about 14% in the specimen thickness was observed. The increased stress triaxiality level occurred in the bulk material away from the

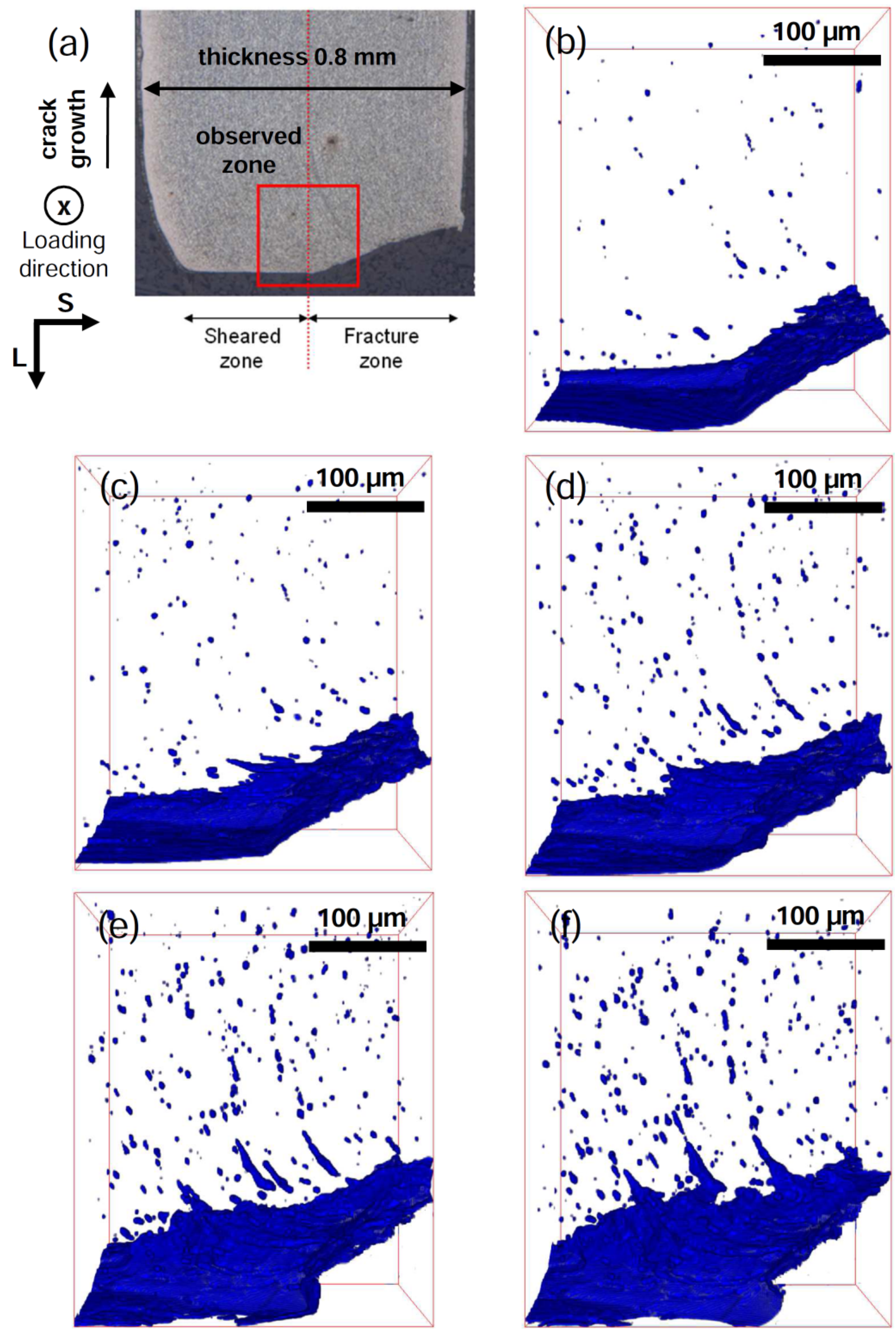

Figure 3.7: 3D volumes of the reconstructed laminography data showing a region of $330\times400\times200\mu m^3$ in the L-S plane at mid-thickness of the damage evolution from a punched edge at different CMODs. Voids, specimen surface and the crack are shown in blue. The steel matrix is made transparent (a) schematic view illustrating specimen geometry, observed area location and loading and crack growth directions; (b) material at delivery state; (c) CMOD $= 2mm$; (d) CMOD$=3mm$; (e) CMOD$=4mm$; (f) CMOD$=4.5mm$.

edge surface was favored by the necking which was of about 40% and 27% at the edge (fig. 3.9(c) when CMOD is 7.25 mm). This is consistent with the higher damage growth in the bulk material observed in fig. 3.9(e).

For the punched edge, similar 2D sections have been examined and at crack initiation no necking was

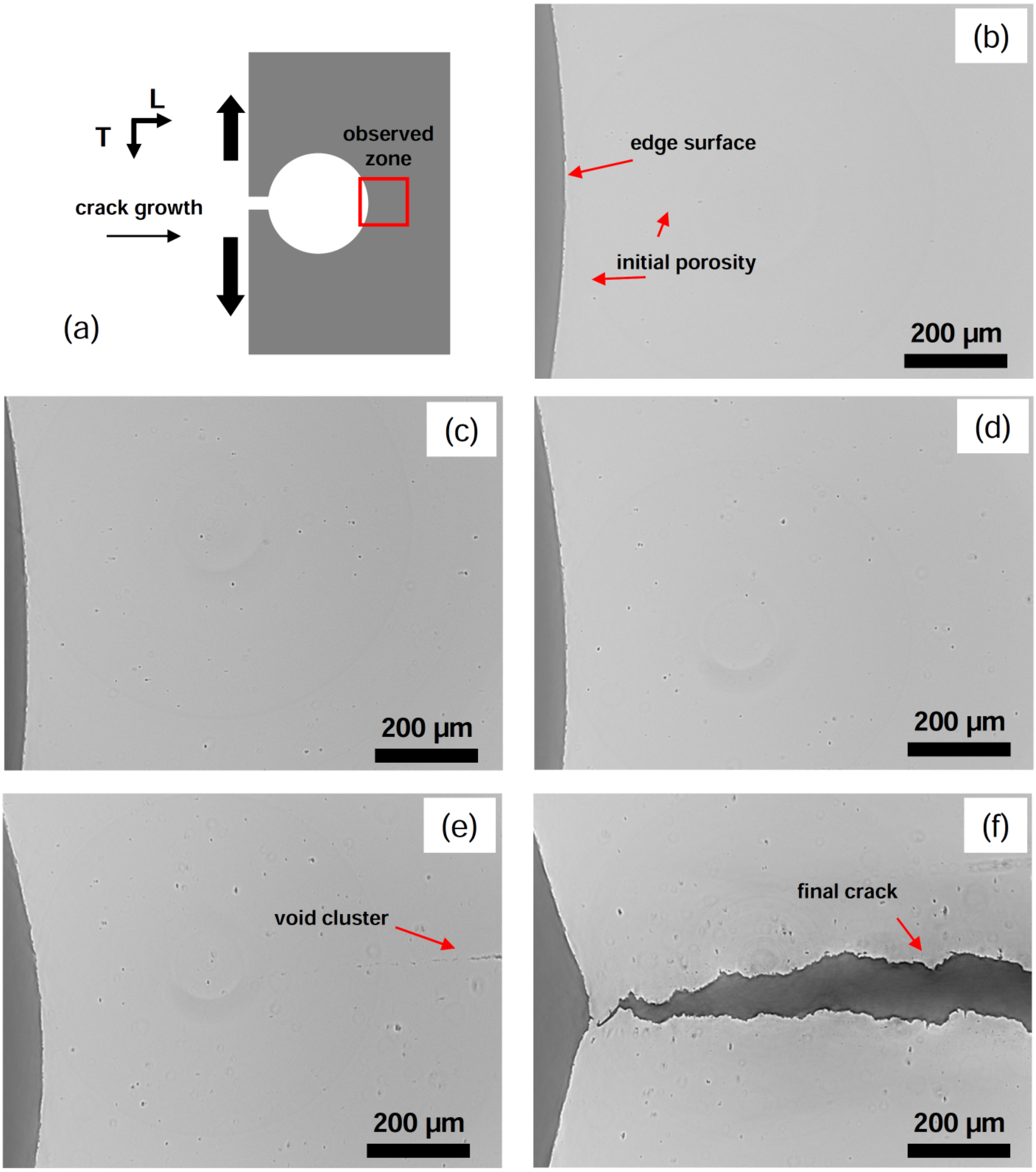

Figure 3.8: 2D sections taken at mid-thickness of reconstructed laminography data showing damage evolution from a machined edge at differents CMODs (a) schematic drawing illustrating specimen geometry, ROI location and loading and crack growth directions (b) material at delivery state; (c) CMOD=3mm; (d) CMOD=6.25mm; (e) CMOD=7.25mm; (f) CMOD=7.75mm.

found ahead of the edge.

3.3 Quantitative analysis of damage evolution

Using the in-house code based on Python freeware, X-ray synchrotron laminography data were quantitatively analyzed. Fig. 3.11 shows the void volume fraction evolution, $< max_T(VVF) >_S$, in the L

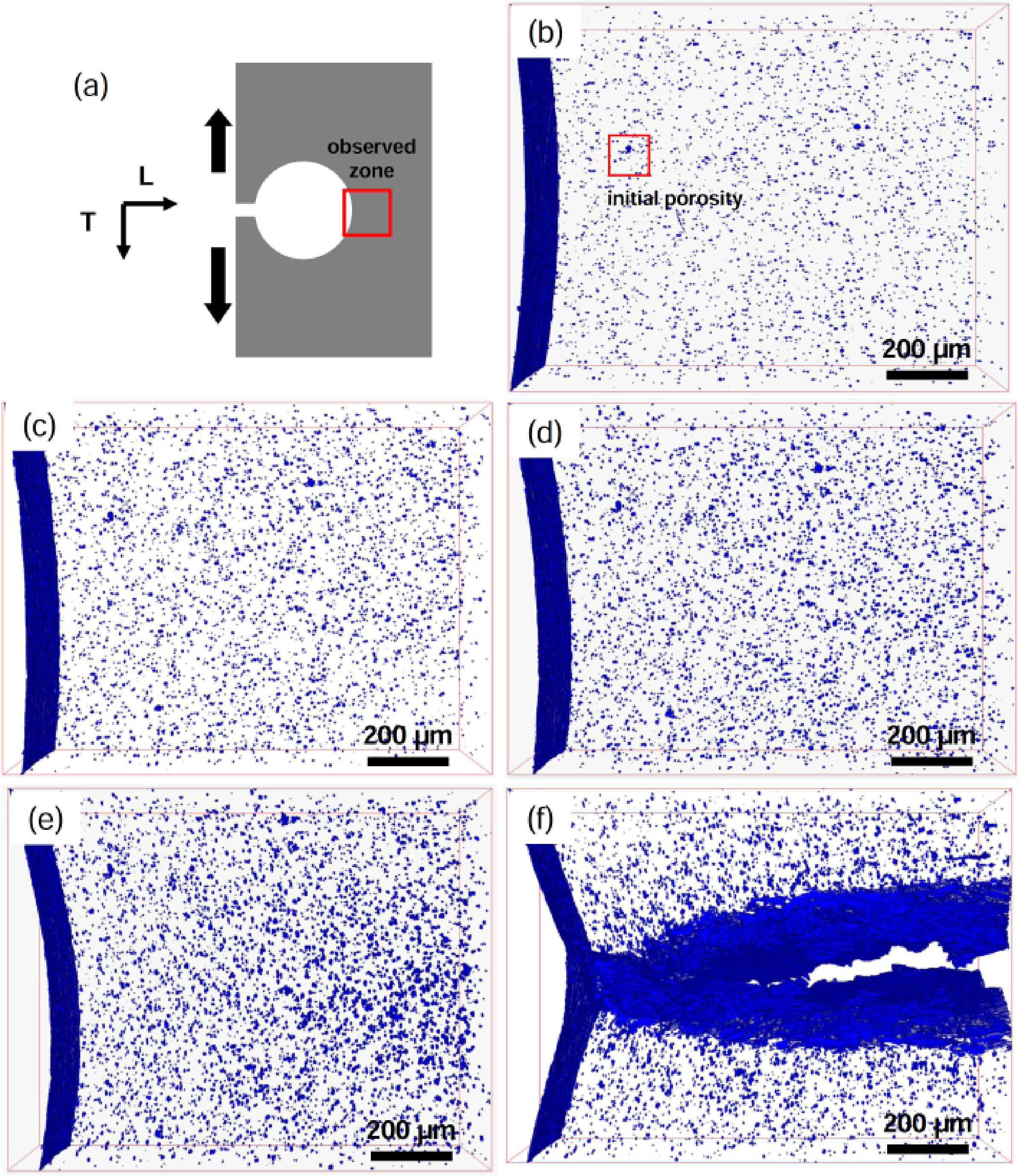

Figure 3.9: 3D volumes of the reconstructed laminography data showing a region of $1240 \times 930 \times 310$ μm^3 in the L-T plane at mid-thickness of the damage evolution from a machined edge at different CMODs. Voids, specimen surface and the crack are shown in blue. The steel matrix is made transparent (a) schematic drawing illustrating specimen geometry, observed area location and loading and crack growth directions; (b) material at delivery state; (c) CMOD = $3mm$; (d) CMOD=$6.25mm$; (e) CMOD=$7.25mm$; (f) CMOD=$7.75mm$ (final crack).

direction from the edge surface. For the punched edge the evolutions plotted correspond to the initial state, CMOD=$2mm$, CMOD=$3mm$, CMOD=$4mm$ and CMOD=$4.5mm$. At the initial state of the punched edge, the $< max_T(VVF) >_S$ was of about 0.2% in the region situated at $200\mu m$ close to the edge surface and of 0.1% away from it, this is consistent with the litterature value [1] in terms of distance. During notch opening, the $< max_T(VVF) >_S$ increases close to the edge surface. It reaches approximatively

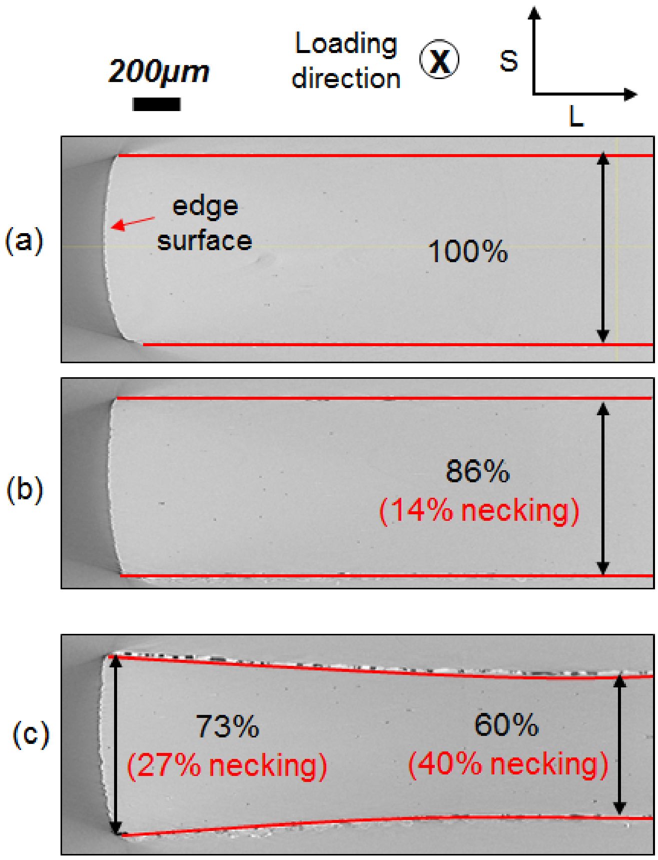

Figure 3.10: 2D sections taken at the minimum L-S sections of reconstructed laminography data of damage evolution from a machined edge at differents CMODs: (a) material at delivery state; (b) CMOD=5.5mm; (c) CMOD=7.25mm. The specimen border was redrawn in red to improve clarity

0.35% at CMOD=3mm, 0.45% at CMOD=4mm and 0.55% at CMOD=4.5mm. The maximum values shown for the CMOD=4.5mm for the punched edge are measured close to the formed crack tip. This is in agreement with the results shown in (fig. 3.6), the void growth in the punched edge was higher close to the edge surface than in the bulk material.

The 3D sub-volumes of the machined edge analyzed correspond to the initial state, CMOD=5.5mm, CMOD=6.25mm and CMOD=7.25mm. In the machined edge at the initial state after machining, the VVF measured was of about 0.1% across all the specimen thickness. As shown in fig. 3.9(b) the voids present in the DP600 bulk material are homogeneously distributed. At CMOD=5.5 and 6.25mm, the $< max_T(VVF) >_S$ measured is between 0.3 and 0.4%. The $< max_T(VVF) >_S$ measured in the machined edge at CMOD=7.25mm has reached more than 1% in the bulk material, however close to the edge surface the measured VVF was of about 0.35%. This was explained in 3.2 by the increased stress triaxiality generated away from the edge surface induced by necking in this area and thus the increased void density seen in fig. 3.9(e).

4 Numerical analysis

To interpret further the present results in particular the crack initiation location for the punched and the machined edge some finite element simulations are carried out in this section.

DOI: 10.1007/s11340-015-0076-3

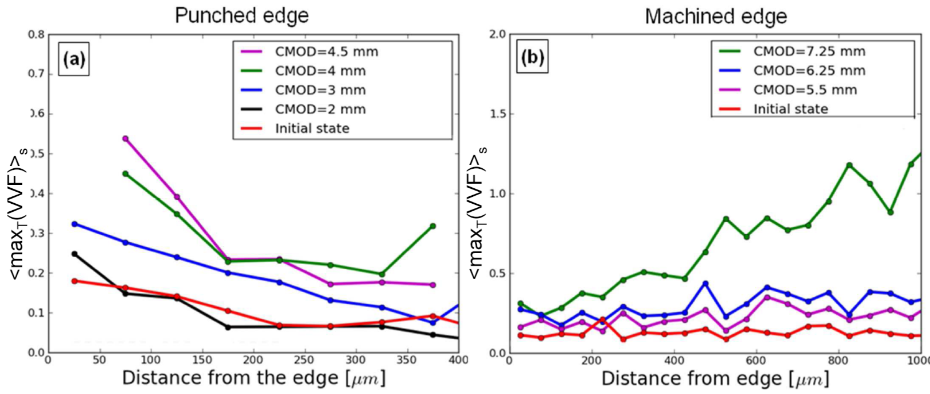

Figure 3.11: Average of maximum void volume fraction values evolution at different CMODs: (a) punched edge. (b) machined edge

4.1 The material behavior

The invariant stress and strain rate measures $\underline{\sigma}$ and $\underline{\dot{\varepsilon}}$ are defined by transport of the Cauchy stress $\underline{\mathbf{T}}$ and strain rate $\underline{\mathbf{D}}$ into the corotational frame characterized by the rotation $\underline{\mathbf{Q}}(\underline{\mathbf{x}},\mathbf{t})$. This change of frame takes place at each material point:

$$\begin{cases} \underline{\sigma} = \underline{Q} \cdot \underline{T} \cdot \underline{Q}^T, \\ \underline{\dot{\varepsilon}} = \underline{Q} \cdot \underline{D} \cdot \underline{Q}^T, \\ \underline{Q} \ such \ as \ \underline{\dot{Q}}^T \cdot \underline{Q} = \underline{\Omega} \ \text{(corotational)}, \end{cases} \tag{2}$$

where $\underline{\Omega}$ is the skew-symmetric part of the gradient $\underline{\mathbf{L}}$ of the velocity field [72]. The strain rate tensor $\underline{\dot{\varepsilon}}$ is split into elastic and plastic contributions, the evolution of the latter being given by the plastic flow rule.

$$\underline{\dot{\varepsilon}} = \underline{\dot{\varepsilon}}_e + \underline{\dot{\varepsilon}}_p \tag{3}$$

$$\underline{\sigma} = \underline{\underline{E}} . \underline{\varepsilon}_e \tag{4}$$

$$f(\underline{\sigma}, p) = J_2(\underline{\sigma}) - R(p) \tag{5}$$

$$\underline{\dot{\varepsilon}}_p = \dot{p} \frac{\partial f}{\partial \underline{\sigma}} = \frac{3}{2} \frac{\underline{s}}{J_2(\underline{\sigma})} \tag{6}$$

where $J_2(\underline{\sigma})$ is the Von Mises invariant of the stress tensor, $\underline{\mathbf{s}}$ is the deviatoric part of the stress tensor $\underline{\sigma}$, $R(p)$ is the non-linear hardening law. A Non-linear (Armstrong-Frederick type) kinematic hardening was included in the model using two back-stresses [73].

$$\underline{X} = \underline{X}_1 + \underline{X}_2 \tag{7}$$

$$with \ \ \underline{\dot{X}}_1 = \frac{2}{3} C_1 \underline{\dot{\varepsilon}}_p - \dot{p} D_1 \underline{X}_1 \ \ and \ \ \underline{\dot{X}}_2 = \frac{2}{3} C_2 \underline{\dot{\varepsilon}}_p - \dot{p} D_2 \underline{X}_2 \tag{8}$$

where C_1, D_1, C_2 and D_2 are materials parameters. An isotropic hardening function $R(p)$ was chosen.

DOI: 10.1007/s11340-015-0076-3

$$R(p) = R_0 + Q(1 - \exp(-bp)) \tag{9}$$

Table 1 shows the optimised material parameters of the investigated DP600 laboratory steel that reproduce very well tensile and reverse shearing curves (fig. 4.12). Reverse shearing corresponds to in plane shearing where the shearing direction is inverted at a given strain [74]. These material parameters are identified using unpublished tensile and reverse shearing tests performed at ArcelorMittal Global R&D for the material of our study.

Table 1: Optimised material parameters for constitutive equations (DP600)

R_0 $[MPa]$	Q $[MPa]$	b	D_1	C_1 $[MPa]$	D_2	C_2 $[MPa]$
217.49	273.54	23.192	2.3577	767.4	154.65	29993.5

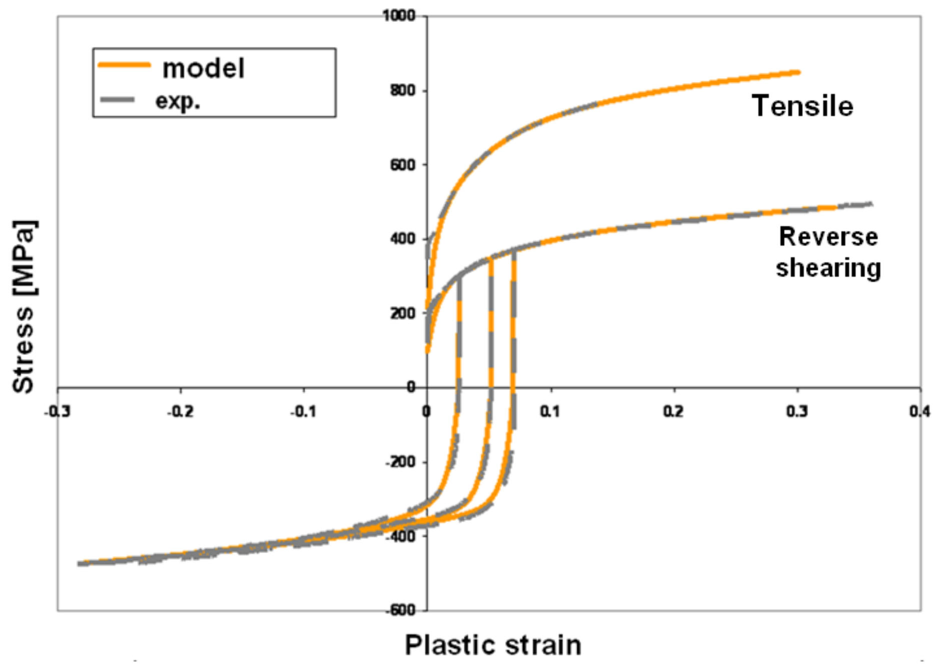

Figure 4.12: True tensile stress-strain and reverse shearing curves obtained for the investigated DP600 laboratory steel

4.2 Digital image correlation and finite elements analysis

Using the simple 2 screws loading device (see fig. 2.3(a) and also [63]), the displacements applied on the specimen ROI were not known. The ROI is quite small compared with the whole specimen dimensions. A multiscale analysis was then proposed to simulate only the ROI (fig. 4.14). A 2D plane-stress finite element analysis had been carried out using the Z-set® software on the whole specimen geometry in order to extract the displacement fields around the punched and the machined edge that will be used as input data for the computation cost optimized 3D elasto-plastic simulations (fig. 4.13(c)). The displacements of the points A and B, corresponding to the upper corners of the ROI used for DIC (fig. 4.13(c)) were calculated and compared to the ones measured using DIC.

Surface digital image correlation (DIC) was performed using Correli^{Q4} on the ROI images taken on the in situ laminography specimen surface in order to determine precisely the real displacements applied to the edges. Fig. 4.13(a) shows the displacement of the upper side of the correlation box measured at CMOD=$2mm$ in the T-direction. The DIC allowed to conclude that the upper and bottom correlation box sides moved symmetrically in the T-direction with respect to the middle axis (dotted line black in fig. 4.13(a)). We observed that during plastic deformation, all the upper side nodes and the right side nodes remained aligned at different CMODs in the T-direction and L-direction respectively. The affine functions corresponding to these aligned displacement of the upper and the right side of the correlation box in the L and T directions were thus determined. The plot in fig. 4.13(b) gives the upper side nodes displacements (dots) on the punched edge ROI surface and the corresponding function fitted measured at CMOD= 1, 2, 3 and $4mm$ in the T-direction. There was a good agreement between the 2D finite element simulation and the surface digital correlation (fig. 4.13(d)).

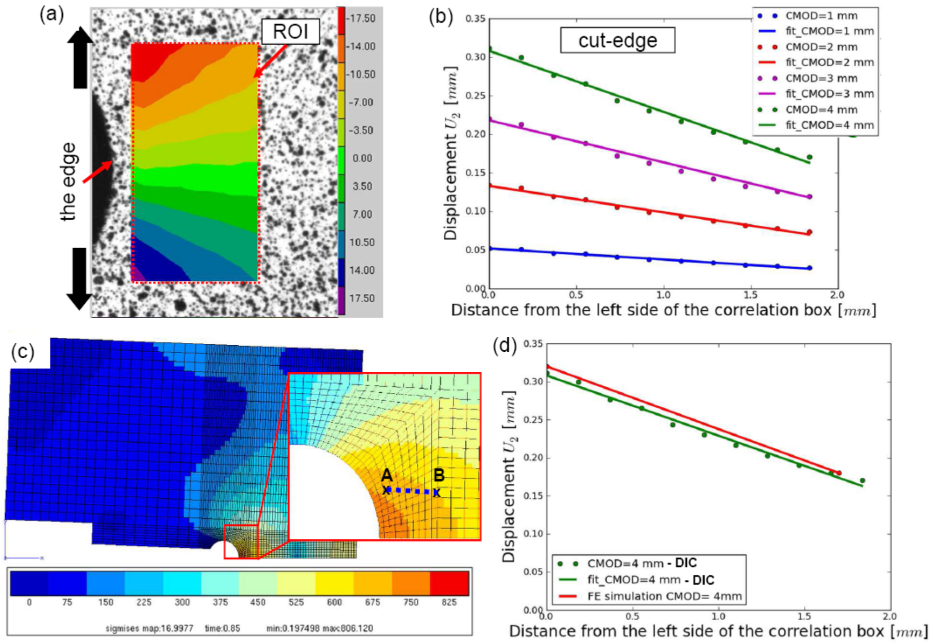

Figure 4.13: (a) Displacement fields cartography of the punched edge at CMOD=$2mm$ measured by DIC; (b) Displacement of the top side of the correlation box of the punched edge at different CMODs; (c) Von Mises stress cartography calculated by 2D FE analysis on the laminography specimen; (d) the correlation box top side displacement found by DIC and 2D FE analysis.

The constitutive law described in 4.1 was used to simulate the wedge opening in order to assess the difference between the punched edge and the machined edge behaviors. The boundary conditions applied for the 3D finite element analysis on the meshes showed in fig. 4.14 were obtained from the 2D simulation and they are:

- Left $U_L(x,t) = (A_1.y + B_1)t$
- Right $U_L(x,t) = (A_2.y)t$
- Top $U_T(y,t) = (A_3.x + B_3)t$
- Bottom $U_T = 0$ (symmetry)

Where A_1, A_2, A_3, B_1 and B_3 are constants identified using 2D FE simulation. The values of these constants are given in the table 2.

The 3D analysis was performed in order to understand the influence of the edge profile resulting from the punching process on the stress triaxiality distribution and study the behavior of cut and machined

DOI: 10.1007/s11340-015-0076-3

Table 2: Boundary conditions constants for 3D finite element simulation.

	A1	B2	A2	A3	B3
Punched edge	0.25	-0.058	0.022	-0.12	0.048
Machined edge	0.26	-0.058	0.017	-0.11	0.042

edges. The stress triaxiality ratio is defined as: $\tau = \frac{1}{3}\sigma_{kk}/\sigma_{eq}$, where σ_{kk} is the trace of the stress tensor and σ_{eq} the von Mises equivalent stress. In addition to the edge profile, the work hardening caused by the punching process in the adjacent region to the punched edge face was taken into account through the accumulated plastic strain $p_0 = p(t=0)$. This allowed us to understand hardening of the cutting affected zone observed in 2.2(b) ($400\mu m$). The affected zone in the punched edge is shown in fig. 4.14(a). It consists of eight rows of elements of $50\mu m$ corresponding to the colored regions in fig. 4.14(a). The accumulated plastic strain values introducing the work hardening of the affected zone have been taken from the punched edge hardening profile seen in 2.2(b). It was introduced as follows:

- 1st row of elements (the punched edge surface) $ep_{cum} = 48\%$
- 2nd row $ep_{cum} = 42\%$ ($\sim$50 μm from edge)
- 3rd row $ep_{cum} = 36\%$ ($\sim$100 μm from edge)
- 4th row $ep_{cum} = 30\%$ ($\sim$150 μm from edge)
- 5th row $ep_{cum} = 24\%$ ($\sim$200 μm from edge)
- 6th row $ep_{cum} = 18\%$ ($\sim$250 μm from edge)
- 7th row $ep_{cum} = 12\%$ ($\sim$300 μm from edge)
- 8th row $ep_{cum} = 6\%$ ($\sim$350 μm from edge)

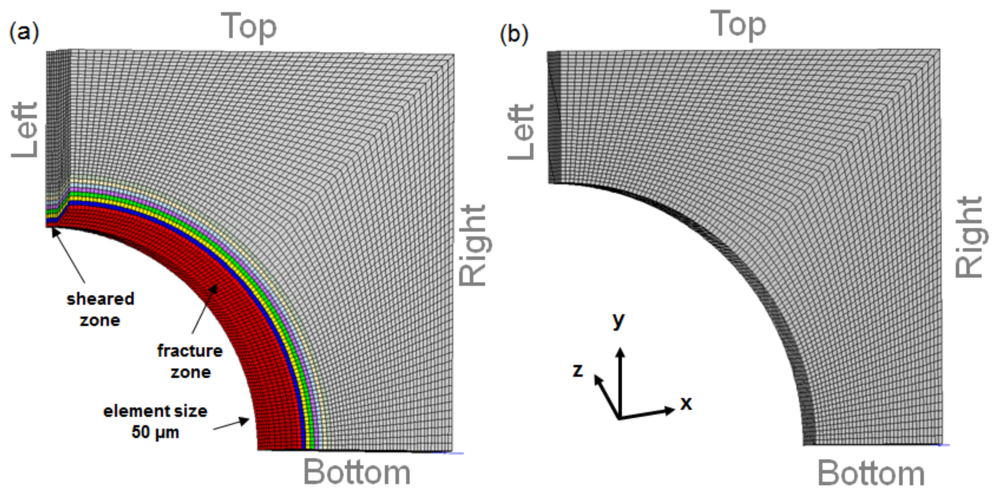

Figure 4.14: Full thickness meshes of the investigated zone used for the 3D FE analysis: (a) 3D mesh of the punched edge taking into account the affected zone (with colors); (b) 3D mesh of the machined edge.

The stress triaxiality and the accumulated plastic strain were extracted from FE simulations in order to understand the link between these local mechanical parameters and the edges behaviors. The fig. 4.15

DOI: 10.1007/s11340-015-0076-3

shows the the stress triaxiality level and the accumulated plastic strain calculated for the prestrained punched edge, the punched edge and the machined edge at CMOD= $4.5mm$. An increased level of stress triaxiality and accumulated plastic strain was found in the material bulk.

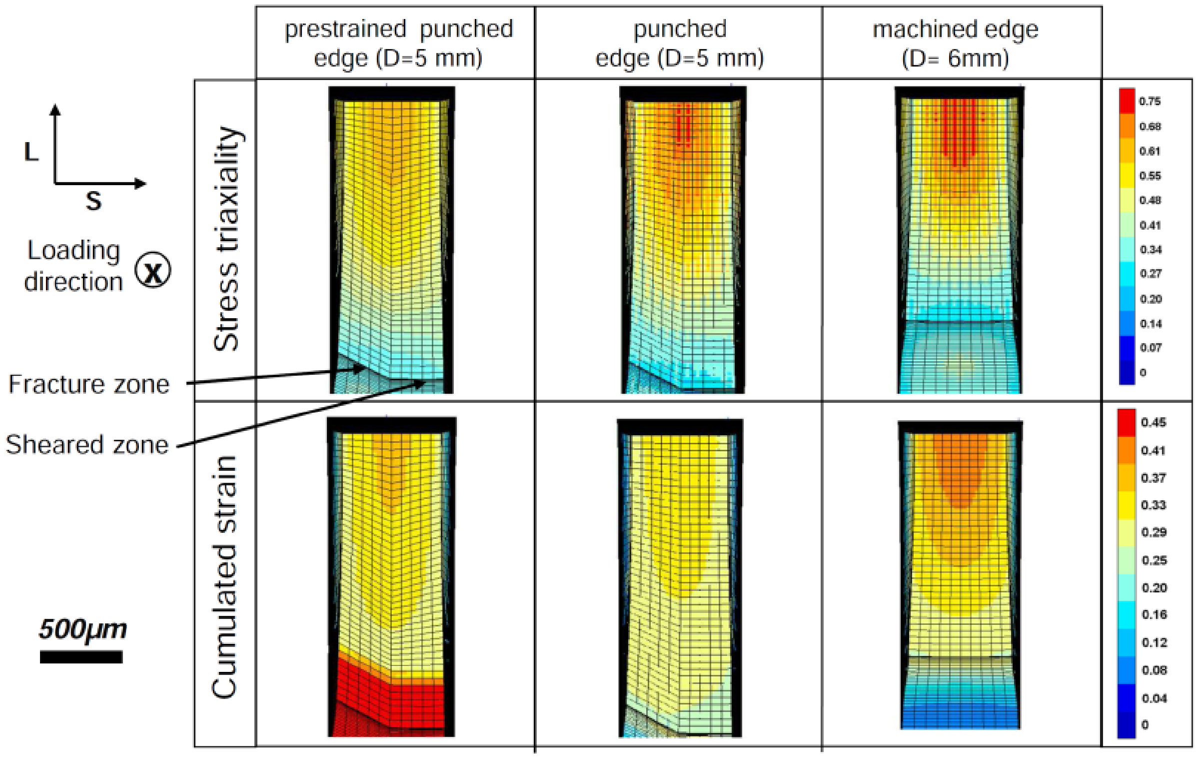

Figure 4.15: Stress triaxiality and accumulated plastic strain in prestrained punched-edge, punched-edge and machined-edge found at CMOD=$4.5mm$.

The fig. 4.16 shows the evolution of the stress triaxiality and the accumulated plastic strain at mid-thickness. Stress triaxiality ratio is defined here as the hydrostatic pressure divided by the Von Mises equivalent stress. The accumulated plastic strain in the prestrained punched edge is higher close to the edge surface than away from it. This is due to the initial plastic strain introduced to take into account the hardening of the affected zone. Ahead of the edge, there is no difference between the behaviors of the prestrained punched edge and the punched edge. The machined edge presents an increased level of stress triaxiality and accumulated plastic strain compared to the two other investigated edges.

The necking for the three investigated edge configurations always occurs far from the edge. This is consistent with the experimental results obtained for the machined edge. However, it does not allow to predict the punched edge behavior.

5 Discussion

The laminography observations have revealed a drastic change of damage mechanisms for the two investigated edges.

In [46], it was found that during hole expansion, cracks were mainly initiated at the fracture zone surface. We have clearly observed in 3D that for the studied DP laboratory steel the fracture zone is rough and the damage caused by the punching process in the fracture zone is in the form of needle voids. These needle voids grow from the fracture zone surface following the ferrite/martensite flow lines. The punched edge fracture is mainly governed by the growth of the needle voids. This may be explained by the increased

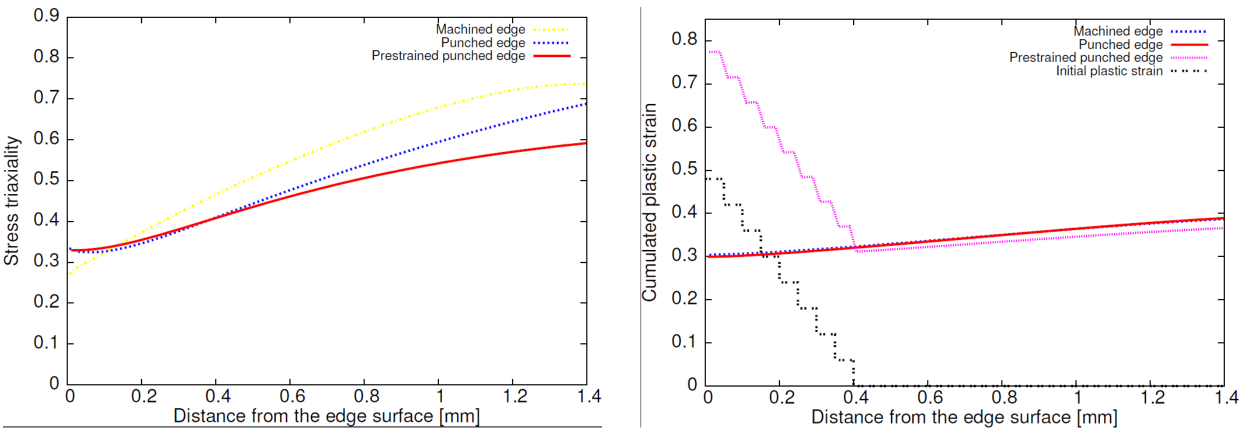

(a) (b)

Figure 4.16: Evolution of stress triaxiality (a) and cumulated plastic strain (b) in prestrained punched-edge, punched-edge and machined-edge at CMOD=4.5mm at mid-thickness.

level of stress triaxiality generated in the needle voids tip and the prestrained ferrite/martensite interfaces in the cutting affected zone. However, an increased damage initiation and growth was observed in the bulk material during machined edge loading that has undergone substantial necking. The resolution has an important influence on the damage measurement [69]. It would be interesting to carry out an in situ SEM observations on the sample surface in order to detect the damage mechanisms at high resolution.

The finite element analysis using elasto-plastic constitutive law has shown that the bulk material has undergone an increased stress triaxiality for the punched and the machined edge. These results allow us to explain the behavior of the machined edge observed using X-ray laminography. It would be interesting to perform the same simulations using models that take into account the initial damage and the stress triaxiality in order to understand the influence of the edge profile and the necking on the edge behavior.

6 Conclusions

The experimental study and numerical simulations presented in this paper aim at characterizing the initial damage state and subsequent damage evolution during mechanical loading from DP600 steel grade cut-edges: 1) a *punched edge* and 2) a *machined and finely ground edge.*

3D imaging using synchrotron radiation computed laminography has allowed us to identify different defects that a *punched edge* contains at the initial state. These include: roughness in the fracture zone, needle-shape voids in the bulk from fracture zone and alignment of needle voids along the flow lines i.e. martensite alignments. The 3D in situ laminography observation carried out on a sample with a circular punched hole has allowed us to characterize, for the first time, the damage evolution from a cut-edge in situ and in 3D during mechanical loading. The novelty of high energy synchrotron laminography is that regions of interests in large flat steel specimens can be investigated. Due to this possibility, boundary conditions close to those encountered during metal sheet forming are applied here. The growth of needle voids was especially along flow lines from fracture zone surface but also in the bulk along the martensite alignments. The initial void growth direction corresponds thus to the S direction (thickness). We observe that the coalescence of needle voids from the fracture zone with the sheared zone occurs via narrow coalescence zones (void sheets). These cracks are inclined by 45° compared to the L-direction. Several cracks are formed, especially in the fracture zone, but the one located close to a geometrical defect grows faster.

In contrast, for the case of the machined edge, the damage does not start from the edge but in the material

DOI: 10.1007/s11340-015-0076-3

bulk that has undergone substantial necking during loading. The local necking appearing away from the edge is accompanied with an increased damage accumulation that leads to the final crack.

3D image analysis was performed to quantify the damage at initial state and its evolution during mechanical loading. A slightly increased level of void volume fraction was measured close to the punched edge surface (in the punching-affected zone). The damage starts in a very localized way from the fracture zone (needle-shape voids) because cutting strongly weakens the materiallocally.

2D image correlation and 3D FE simulations were perfomed to interpret the edge behavior in terms of mechanical fields. Using an elasto-plastic constitutive law, it is was found for the punched edge that:

- Meshing the edge profile geometry does not allow to localise the stress triaxiality and plastic strain in the edge region.
- Numerically accounting for the pre-straining introduced in the cutting-affected zone does not localize strain and triaxiality in the edge region either.

In contrast, the behavior of the machined edge observed experimentally can be reproduced in the simulation. The stress triaxiality and the plastic strain are localized in the simulation far ahead of the edge which is consistent with the increased level of void growth in the machined edge observed during in situ laminography experiment. To interpret and reproduce the mechanical behavior at the punched edge, more sophisticated models taking into account the roughness of the fracture zone, damage nucleation kinetics for different stress states, the initial porosity and the damage anisotropy should be used.

Acknowledgements

The authors would like to thank ArcelorMittal Global R&D for financial support and material supply and Astrid Perlade for helpful discussions. The authors also acknowledge the ESRF for the provision of synchrotron radiation at ID19 beam-line through the MA1631 project.

References

[1] A. Dalloz, J. Besson, A.-F. Gourgues-Lorenzon, T. Sturel, and A. Pineau. Effect of shear cutting on ductility of a dual phase steel. *Engineering Fracture Mechanics*, 76(10):1411–1424, 2009.

[2] Daniel J. Thomas. Effect of mechanical cut-edges on the fatigue and formability performance of advanced high-strength steels. *Journal of Failure Analysis and Prevention*, 12(5):518–531, 2012.

[3] A. Lara, I. Picas, and D. Casellas. Effect of the cutting process on the fatigue behaviour of press hardened and high strength dual phase steels. *Journal of Materials Processing Technology*, 213:1908–1919, 2013.

[4] M. Mazinani and W.J. Poole. Effect of martensite plasticity on the deformation behavior of a low-carbon dual-phase steel. *Metallurgical and Materials Transactions A*, 38(2):328–339, 2007.

[5] E. Maire, O. Bouaziz, M. Di Michiel, and C. Verdu. Initiation and growth of damage in a dual-phase steel observed by x-ray microtomography. *Acta Materialia*, 56(18):4954–4964, 2008.

[6] C. Landron, O. Bouaziz, E. Maire, and J. Adrien. Characterization and modeling of void nucleation by interface decohesion in dual phase steels. *Scripta Materialia*, 63(10):973–976, 2010.

DOI: 10.1007/s11340-015-0076-3

[7] G. Avramovic-Cingara, Ch.A.R. Saleh, M.K. Jain, and D.S. Wilkinson. Void nucleation and growth in dual-phase steel 600 during uniaxial tensile testing. *Metallurgical and Materials Transactions*, 40(13):3117–3127, 2009.

[8] J. Kadkhodapour, A. Butz, and S. Ziaei Rad. Mechanisms of void formation during tensile testing in a commercial, dual-phase steel. *Acta Materialia*, 59(7):2575–2588, 2011.

[9] M Azuma, S Goutianos, N Hansen, G Winther, and X Huang. Effect of hardness of martensite and ferrite on void formation in dual phase steel. *Materials Science and Technology*, 28(9-10):1092–1100, 2012.

[10] A. Ramazani, A. Schwedt, A. Aretz, U. Prahl, and W. Bleck. Characterization and modelling of failure initiation in dpsteel. *Computational Materials Science*, 75:35–44, 2013.

[11] In-Gyu Park and Anthony W. Thompson. Ductile fracture in spheroidized 1520 steel. *Acta Metallurgica*, 36(7):1653–1664, 1988.

[12] G. Avramovic-Cingara, Y. Ososkov, M.K. Jain, and D.S. Wilkinson. Effect of martensite distribution on damage behaviour in dp600 dual phase steels. *Materials Science and Engineering*, 516:7–16, 2009.

[13] C. Landron, O. Bouaziz, E. Maire, J. Adrien, et al. Experimental investigation of void coalescence in a dual phase steel using x-ray tomography. *Acta Materialia*, 61(18):6821–6829, 2013.

[14] M. Brown and D. Embury. A model of ductile fracture in two-phase materials. In *The 3rd international conference on strength of metals and alloys*, pages 164 – 169, London, 1973.

[15] P.F. Thomason. *Ductile Fracture of Metals*. Pergamon Press, 1990.

[16] A.S. Argon, J. Im, and R. Safoglu. Cavity formation from inclusions in ductile fracture. *Metallurgical Transactions*, 6(4):825–837, 1975.

[17] F.M. Beremin. Cavity formation from inclusions in ductile fracture of a508 steel. *Metallurgical Transactions A*, 12(5):723–731, 1981.

[18] C.C. Chu and A. Needleman. Void nucleation effects in biaxially stretched sheets. *Journal of Engineering Materials and Technology*, 102(3):249–256, 1980.

[19] J.R. Rice and D.M. Tracey. On the ductile enlargement of voids in triaxial stress fields. *Journal of the Mechanics and Physics of Solids*, 17(3):201–217, 1969.

[20] Y Huang. Accurate dilatation rates for spherical voids in triaxial stress fields. *Journal of Applied Mechanics*, 58(4):1084–1086, 1991.

[21] A.L. Gurson. *Continuum Theory of Ductile Rupture by Void Nucleation and Growth: Yield criteria and flow rules for porous ductile media*. Technical report (Brown University. Division of Engineering). Division of Engineering, Brown University, 1975.

[22] Mohamed Ben Bettaieb, Xavier Lemoine, Olivier Bouaziz, Anne Marie Habraken, and Laurent DuchÃne. Numerical modeling of damage evolution of dp steels on the basis of x-ray tomography measurements. *Mechanics of Materials*, 43(3):139–156, 2011.

[23] Joseph Fansi, Tudor Balan, Xavier Lemoine, Eric Maire, Caroline Landron, Olivier Bouaziz, Mohamed Ben Bettaieb, and Anne Marie Habraken. Numerical investigation and experimental validation of physically based advanced {GTN} model for {DP} steels. *Materials Science and Engineering: A*, 569:1–12, 2013.

[24] J. Besson. Continuum models of ductile fracture: A review. *International Journal of Damage Mechanics*, 19(1):3–52, 2010.

[25] Thomas Pyttel, Ralf John, and Michael Hoogen. A finite element based model for the description of aluminium sheet blanking. *International Journal of Machine Tools and Manufacture*, 40(14):1993–2002, 2000.

[26] Z.H. Chen, C.Y. Tang, and T.C. Lee. An investigation of tearing failure in fine-blanking process using coupled thermo-mechanical method. *International Journal of Machine Tools and Manufacture*, 44:155–165, 2004.

[27] Xin Wu, Hamed Bahmanpour, and Ken Schmid. Characterization of mechanically sheared edges of dual phase steels. *Journal of Materials Processing Technology*, 212(6):1209–1224, 2012.

[28] Hyunwoo So, Dennis FaAmann, Hartmut Hoffmann, Roland Golle, and Mirko Schaper. An investigation of the blanking process of the quenchable boron alloyed steel 22mnb5 before and after hot stamping process. *Journal of Materials Processing Technology*, 212(2):437–449, 2012.

[29] TC Lee, LC Chan, and BJ Wu. Straining behaviour in blanking process - fine blanking vs conventional blanking. *Journal of Materials Processing Technology*, 48:105–111, 1995.

[30] Ridha Hambli. Comparison between lemaitre and gurson damage models in crack growth simulation during blanking process. *International Journal of Mechanical Sciences*, 43(12):2769–2790, 2001.

[31] Ridha Hambli. Prediction of burr height formation in blanking processes using neural network. *International Journal of Mechanical Sciences*, 44(10):2089–2102, 2002.

[32] T.B. Hilditch and P.D. Hodgson. Development of the sheared edge in the trimming of steel and light metal sheet: Part 1, experimental observations. *Journal of Materials Processing Technology*, 169(2):184–191, 2005.

[33] K. Mori, S. Saito, and S. Maki. Warm and hot punching of ultra high strength steel sheet. {*CIRP*} *Annals - Manufacturing Technology*, 57(1):321–324, 2008.

[34] H. So, H. Hoffmann, and R. Golle. Blanking of press hardened ultra high strength steel. In *Proceedings of 2nd International Conference on Hot Sheet Metal Forming of High-performance Steel*, pages 137 – 145, Luleo, Sweden, 2009.

[35] P. Sartkulvanich, B. Kroenauer, R. Golle, A. Konieczny, and T. Altan. Finite element analysis of the effect of blanked edge quality upon stretch flanging of ahss. *CIRP Annals - Manufacturing Technology*, 59(1):279–282, 2010.

[36] K. Mori. Smart hot stamping of ultra-high strength steel parts. *Transactions of Nonferrous Metals Society of China*, 22, Supplement 2(0):s496–s503, 2012.

[37] K. Mori, Y. Abe, Y. Kidoma, and P. Kadarno. Slight clearance punching of ultra-high strength steel sheets using punch having small round edge. *International Journal of Machine Tools and Manufacture*, 65(0):41–46, 2013.

[38] Etienne Taupin, Jochen Breitling, Wei tsu Wu, and Taylan Altan. Material fracture and burr formation in blanking results of {FEM} simulations and comparison with experiments. *Journal of Materials Processing Technology*, 59(1–2):68–78, 1996.

[39] Jochen Breitling, Victor Chernauskas, Etienne Taupin, and Taylan Altan. Precision shearing of billetsspecial equipment and process simulation. *Journal of Materials Processing Technology*, 71(1):119–125, 1997.

[40] A.M Goijaerts, Y.W Stegeman, L.E Govaert, D Brokken, W.A.M Brekelmans, and F.P.T Baaijens. Can a new experimental and numerical study improve metal blanking? *Journal of Materials Processing Technology*, 103(1):44–50, 2000.

[41] A.M. Goijaerts, L.E. Govaert, and F.P.T. Baaijens. Evaluation of ductile fracture models for different metals in blanking. *Journal of Materials Processing Technology*, 110(3):312–323, 2001.

[42] Ji Hoon Kim, M.G. Lee, D. Kim, D.K. Matlock, and R.H. Wagoner. Hole-expansion formability of dual-phase steels using representative volume element approach with boundary-smoothing technique. *Materials Science and Engineering: A*, 527(27–28):7353–7363, 2010.

[43] Gajendra Jha, Sourav Das, Arijit Lodh, and Arunansu Haldar. Development of hot rolled steel sheet with 600 mpa uts for automotive wheel application. *Materials Science and Engineering: A*, 552:457–463, 2012.

[44] M.D. Taylor, K.S. Choi, X. Sun, D.K. Matlock, C.E. Packard, L. Xu, and F. Barlat. Correlations between nanoindentation hardness and macroscopic mechanical properties in {DP980} steels. *Materials Science and Engineering: A*, pages –, 2014.

[45] Kai Wang, Meng Luo, and Tomasz Wierzbicki. Experiments and modeling of edge fracture for an ahss sheet. *International Journal of Fracture*, 187(2):245–268, 2014.

[46] Kohei Hasegawa, Kenji KAWAMURA, Toshiaki URABE, and Yoshihiro HOSOYA. Effects of microstructure on stretch-flange-formability of 980 mpa grade cold-rolled ultra high strength steel sheets. *ISIJ International*, 44 (3):603–609, 2004.

[47] O. Bouaziz, S. Douchamps, L. Durrenberger, and A. Bui-Van. The double bending test: a promising new way for an optimal characterization of cut-edges ductility. In *International Deep-Drawing Research Group*, pages 164 – 169, London, 2010.

[48] B.S. Levy, M. Gibbs, and C.J. Tyne. Failure during sheared edge stretching of dual-phase steels. *Metallurgical and Materials Transactions A*, 44(8):3635–3648, 2013.

[49] B. Levy and C. Van Tyne. Effect of a strain-hardening rate at uniform elongation on sheared edge stretching. *Journal of Materials Engineering and Performance*, pages 1–8, 2012.

[50] B. Levy and C. Van Tyne. Review of the shearing process for sheet steels and its effect on sheared-edge stretching. *Journal of Materials Engineering and Performance*, pages 1–9, 2011.

[51] J. J. Gammage, D. S. Wilkinson *, J. D. Embury, and E. Maire. Damage studies in heterogeneous aluminium alloys using x-ray tomography. *Philosophical Magazine*, 85(26-27):3191–3206, 2005.

[52] Eric Maire, Cyril Bordreuil, Laurent Babout, and Jean-Claude Boyer. Damage initiation and growth in metals. comparison between modelling and tomography experiments. *Journal of the Mechanics and Physics of Solids*, 53(11):2411–2434, 2005.

[53] Eric Maire, Suxia Zhou, Jerome Adrien, and Marco Dimichiel. Damage quantification in aluminium alloys using in situ tensile tests in x-ray tomography. *Engineering Fracture Mechanics*, 78(15):2679–2690, 2011.

[54] C. Landron, E. Maire, O. Bouaziz, J. Adrien, L. Lecarme, and A. Bareggi. Validation of void growth models using x-ray microtomography characterization of damage in dual phase steels. *Acta Materialia*, 59(20):7564–7573, 2011.

[55] L. Helfen, T. Baumbach, P. Mikulik, D. Kiel, P. Pernot, P. Cloetens, and J. Baruchel. High-resolution three-dimensional imaging of flat objects by synchrotron-radiation computed laminography. *Applied Physics Letters*, 86(7):071915–071915–3, 2005.

[56] L. Helfen, A. Myagotin, A. Rack, P. Pernot, P. Mikulík, M. Di Michiel, and T. Baumbach. Synchrotron-radiation computed laminography for high-resolution three-dimensional imaging of flat devices. *Physica Status solidi A*, 204:2760–2765, 2007.

[57] L. Helfen, A. Myagotin, P. Mikulík, P. Pernot, A. Voropaev, M. Elyyan, M. Di Michiel, J. Baruchel, and T. Baumbach. On the implementation of computed laminography using synchrotron radiation. *Review of Scientific Instruments*, 82(6):–, 2011.

[58] Feng Xu, Lukas Helfen, Andrew J. Moffat, Gregory Johnson, Ian Sinclair, and Tilo Baumbach. Synchrotron radiation computed laminography for polymer composite failure studies. *Journal of Synchrotron Radiation*, 17(2):222–226, 2010.

[59] D.J. Bull, L. Helfen, I. Sinclair, S.M. Spearing, and T. Baumbach. A synthesis of multi-scale 3d x-ray tomographic inspection techniques for assessing carbon fibre composite impact damage. *Composites Science and Technology*, 75:55–61, 2013.

[60] T.F. Morgeneyer, L. Helfen, I. Sinclair, H. Proudhon, F. Xu, and T. Baumbach. Ductile crack initiation and propagation assessed via in situ synchrotron radiation-computed laminography. *Scripta Materialia*, 65(11):1010–1013, 2011.

[61] Yang Shen, Thilo F. Morgeneyer, Jérôme Garnier, Lucien Allais, Lukas Helfen, and Jérôme Crépin. Three-dimensional quantitative in situ study of crack initiation and propagation in {AA6061} aluminum alloy sheets via synchrotron laminography and finite-element simulations. *Acta Materialia*, 61(7):2571–2582, 2013.

[62] T. Ueda, L. Helfen, and T.F. Morgeneyer. In-situ laminography study of three-dimensional individual void shape evolution at crack initiation and comparison with gtn-type simulations. *Accepted for publication in Acta Materialia*, 2014.

[63] T.F. Morgeneyer, L. Helfen, H. Mubarak, and F. Hild. 3d digital volume correlation of synchrotron radiation laminography images of ductile crack initiation: An initial feasibility study. *Experimental Mechanics*, 53(4):543–556, 2013.

[64] W Tong, H Tao, XQ Jiang, NA Zhang, MP Marya, LG Hector, and XHQ Gayden. Deformation and fracture of miniature tensile bars with resistance-spot-weld microstructures. *Metallurgical and materials transactions A-Physical metallurgy and materials science*, 36A(10):2651–2669, OCT 2005.

[65] T. Le Jolu, T. F. Morgeneyer, A. Denquin, M. Sennour, A. Laurent, J. Besson, and A.-F. Gourgues-Lorenzon. Microstructural characterization of internal welding defects and their effect on the plastic behavior of FSW joints of AA2198 Al-Cu-Li alloy. *Metallurgical and Materials Transactions A*, 45:5531–5544, 2014.

[66] P A Douissard, A Cecilia, X Rochet, X Chapel, T Martin, T van de Kamp, L Helfen, T Baumbach, L Luquot, X Xiao, J Meinhardt, and A Rack. A versatile indirect detector design for hard x-ray microimaging. *Journal of Instrumentation*, 7(09):P09016, 2012.

[67] Anton Myagotin, Alexey Voropaev, Lukas Helfen, Daniel Hanschke, and Tilo Baumbach. Efficient volume reconstruction for parallel-beam computed laminography by filtered backprojection on multi-core clusters. *IEEE Transactions on Image Processing*, 22(12):5348–5361, 2013.

[68] M. D. Abramoff, P. J. Magelhaes, and S. J. Ram. Image processing with imagej. *Biophotonics international*, 11(7):36–42, 2004.

[69] C. Landron, E. Maire, J. Adrien, O. Bouaziz, M. Di Michiel, P. Cloetens, and H. Suhonen. Resolution effect on the study of ductile damage using synchrotron x-ray tomography. *Nuclear Instruments and Methods in Physics Research Section B: Beam Interactions with Materials and Atoms*, (0):–, 2011.

[70] T.F. Morgeneyer, J. Besson, H. Proudhon, M.J. Starink, and I. Sinclair. Experimental and numerical analysis of toughness anisotropy in {AA2139} al-alloy sheet. *Acta Materialia*, 57(13):3902–3915, 2009.

[71] F. Hild. A software for displacement field measurements by digital image correlation. *LMT Cachan, report 252.*, 2002.

[72] J. Besson, G. Cailletaud, Chaboche, and Forest S. J.-L. *Non Linear Mechanics of Materials*. Springer, 2010.

[73] J.L. Chaboche. A review of some plasticity and viscoplasticity constitutive theories. *International Journal of Plasticity*, 24(10):1642–1693, 2008.

[74] D. Rèche, J. Besson, T. Sturel, X. Lemoine, and A.F. Gourgues-Lorenzon. Analysis of the air-bending test using finite-element simulation: Application to steel sheets. *International Journal of Mechanical Sciences*, 57(1):43–53, 2012.